Journal of Materials Science & Technology 120 (2022) 253–264

Contents lists available at ScienceDirect

Journal of Materials Science & Technology

journal homepage: www.elsevier.com/locate/jmst

Research Article

Rate-dependent mechanical behavior of single-, bi-, twinned-, and poly-crystals of CoCrFeNi high-entropy alloy

Siyuan Wei [a,*], Yakai Zhao [a,*], Jae-il Jang [b], Upadrasta Ramamurty [a,c]

[a] School of Mechanical and Aerospace Engineering, Nanyang Technological University, 639798, Republic of Singapore
[b] Division of Materials Science and Engineering, Hanyang University, Seoul 04763, Republic of Korea
[c] Technology and Research, Institute of Materials Research and Engineering, Agency for Science, 138634, Republic of Singapore

ARTICLE INFO

Article history:
Received 18 October 2021
Revised 29 November 2021
Accepted 19 December 2021
Available online 3 March 2022

Keywords:
High-entropy alloy
Strain-rate sensitivity
Micropillar compression
Orientation
Nanoindentation

ABSTRACT

While considerable effort is made to understand the solid solution strengthening on the deformation behavior of high-entropy alloys (HEAs), relatively little attention is paid to the role of microstructural interfaces, especially twin boundaries (TBs), on the strain-rate sensitivity (SRS) of them. To address this, we have conducted micropillar compression experiments on single-, bi-, and twinned-crystals of CoCrFeNi HEA and compared the results with those obtained with uniaxial tensile and compression tests on polycrystalline bulk samples. Results show that SRS, as well as the yield strength and plastic flow behavior, in single crystals are orientation dependent due to the differences in the maximum Schmid factors. While the high-angle grain boundaries arrest dislocation motion, TBs allow for dislocation transmission through them, which result in distinct mechanical responses. While the bi-crystal's deformation behavior is controlled by the 'hard' grain, twinned crystals exhibit an 'averaged' response. The large diversity of the reported SRS values in face centered cubic HEAs could be due to the varying fractions and thus contributions of annealing twins in the tested samples.

1. Introduction

High-entropy alloys (HEAs), which are typically complex in composition yet simple in structure, have attracted considerable attention from the research perspective in the recent past [1–3]. Detailed understanding of the plastic deformation mechanisms in these alloys, which contain high concentrations of solutes, is of particular interest [83,84,87]. In this background, the family of equiatomic HEAs with single face-centered cubic (FCC) crystal structure, e.g., CoCrFeMnNi and CoCrFeNi [1,4,5], have received considerable attention as they exhibit unique mechanical attributes, including simultaneously high strength and toughness at low temperatures, high resistance to hydrogen embrittlement, and evident strain-rate sensitivity (SRS) [2,6–9].

Typically, SRS of a material reflects the fundamental nature of the thermally activated deformation process in it. It is quantitatively characterized by the SRS parameter, $m = \frac{\partial \ln \sigma_y}{\partial \ln \dot{\varepsilon}}$, where σ_y is yield strength and $\dot{\varepsilon}$ is the strain rate. In coarse grained (CG) pure metals (grain size, $d > 10$ μm), that have FCC structure (*e.g.*, Ni), m is nearly zero (~0.004). When d is reduced to the nanocrystalline (NC) regime ($d < 100$ nm), a significant enhancement in m (~0.015) is observed [10–14,88]. The $\dot{\varepsilon}$-dependent mechanical responses in the FCC HEAs are different from those of pure FCC metals in two aspects [8,15–17,86]. First, m of CG FCC HEAs is markedly higher (~0.018–0.064) [8,15,18,19], which is attributed to the strong solid solution effect and the high lattice friction stress [17,20], resulting in similar or even slightly higher m than in NC HEAs [8]. Second, a less understood phenomenon is the absence of a clear correlation between d and m in FCC HEAs, unlike that in pure FCC metals, as the reported results are too diverse and sometimes contradictory even. For example, while several studies reported relatively high SRS values for CoCrFeMnNi HEA [17,21], Laplanche et al [22] claimed that SRS of the HEA (~0.007) actually falls in the same range as conventional FCC metals show.

An aspect that is often overlooked in the above context is the role played by different microstructural interfaces, namely grain boundaries (GBs) and twin boundaries (TBs), on the SRS of FCC HEAs. Typically, most FCC HEAs that are examined hitherto are subjected to cold working followed by an annealing treatment. This, combined with their characteristically low stacking fault energies (SFEs) [4,23], generally leads to widely-spread annealing twins to various extents. The effect of such ubiquitous annealing twins on the SRS of FCC HEAs remains largely unexplored.

* Corresponding authors.
E-mail addresses: siyuan007@e.ntu.edu.sg (S. Wei), yakai.zhao@ntu.edu.sg (Y. Zhao).

https://doi.org/10.1016/j.jmst.2021.12.025
1005-0302/

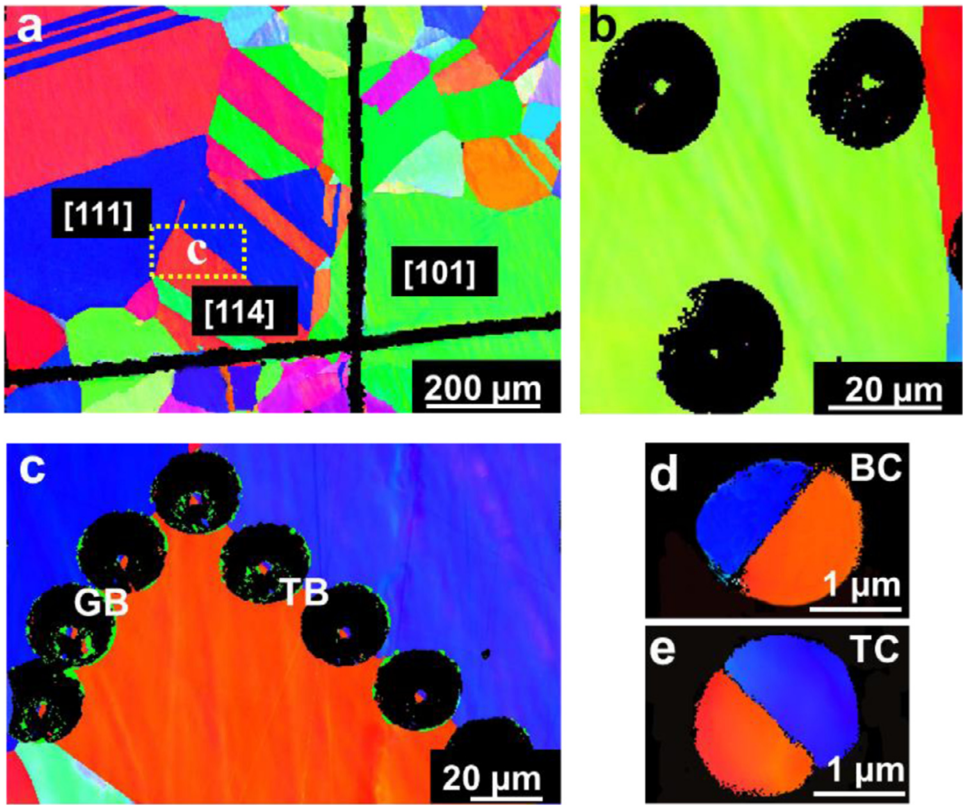

Fig. 1. Representative EBSD micrographs. (a) Area where the micropillars were fabricated. The black unindexed lines are scratch marks utilized to locate the area of interest in FIB and the dashed rectangle marks the area characterized in Fig. 1c. Inverse pole figure (IPF) maps of (b) SC and (c) BC and TC micropillars, with the higher magnification images of the (d) BC and (e) TC pillars.

Keeping the above in view, macroscale uniaxial tensile and compression testing on bulk, polycrystalline (PC) FCC HEA, CoCrFeNi, combined with the micropillar compression testing on single-crystal (SC), bi-crystal (BC) and twinned crystal (TC) samples were conducted and analyzed. The aim is to address the following issues concerning the rate-sensitive deformation of FCC HEA. (1) orientation dependency of SRS in SC HEA micropillars. (2) Influence of GB and TB on the rate-dependent deformation in micropillars and PC samples.

2. Material and methods

The equiatomic CoCrFeNi HEA ingots examined in this study were fabricated by vacuum induction melting of the constituent elements (purity ≥ 99.9 wt.%) and drop casting. The as-cast samples were sequentially hot-rolled at 1050 °C (thickness reduction ~64%), homogenized for 1 h at 1100 °C, cold rolled to reduce the thickness by ~60%, and finally annealed for 1 h at 1100 °C. The microstructures of the samples that were cut and polished (mirror finished using 0.04 μm colloidal silica suspension) were characterized using a scanning electron microscope (SEM, JEOL 7800F) equipped with backscattered electron (BSE) and electron backscatter diffraction (EBSD) probes.

All the mechanical property characterization reported in this paper was performed at room temperature (~25 °C) with the loading direction always parallel to the rolling direction (RD), as schematically illustrated in Fig. S1(a) of the Supplementary Information (SI). The tensile tests on PC samples were conducted using flat dog-bone shaped samples, whose gage length, thickness, and width are 6, 1, and 2 mm, respectively. Compression tests on PC specimens were conducted using cylinder samples with the diameter and height of 2.5 and 5 mm, respectively. Both tensile and compressive tests were performed at the nominal strain rates, $\dot{\varepsilon}$, of 10^{-4}, 10^{-3}, and 10^{-2} s^{-1}. At least five samples were tested at each $\dot{\varepsilon}$. A laser extensometer was used for measuring the strain during tensile tests.

With the aid of orientation maps obtained using EBSD (Fig. 1), micro-scale SC cylindrical pillars with the diameters of ~ 2 μm, height-to-diameter ratio of 2–3, a taper angle that is always below 2°, and crystallographic orientations of [111], [101] and [114] were fabricated using focused ion beam (FIB, Zeiss X540). A three-step milling process (15 and 1.5 nA, followed by 50 pA current) was utilized. The crystallographic orientation dependence of the Schmid factor (SF) is shown in Fig. S1(b) of the Supplementary Information (SI) with the three target orientations marked on it. Additionally, micropillars that either contain a GB or a TB were also fabricated (see Fig. 1). These will be referred to as BC and TC pillars, hereafter. Note that both share the same orientation combinations, i.e., [111] and [114]. The GB in the BC pillar is a high-angle grain boundary (HAGB) with a misorientation of 35.3°. Representative SEM images of the SC, BC, and TC micropillars are displayed in Fig. 2(a–c) respectively.

Uniaxial compression tests were performed on the micropillars using a nanoindentation system (Bruker Hysitron TI980) equipped with a flat punch diamond indenter. Displacement-control mode was utilized to achieve the nominal strain rates, $\dot{\varepsilon}$ (= $(dh/dt)/h$, where h is pillar height and t is time) of 10^{-3}, 5×10^{-3}, and 10^{-2} s^{-1}, respectively. Note that nanoindentation tests at 10^{-4} s^{-1} were not performed, as they require more than 1000 s for completion, and hence are likely to be adversely affected by creep of the pillars and/or thermal drift of the instrument. At least 8 tests were conducted for each condition to examine and ensure reproducibility. The deformed pillars were imaged using SEM after the completion of the tests. Most of the measured stress-strain responses

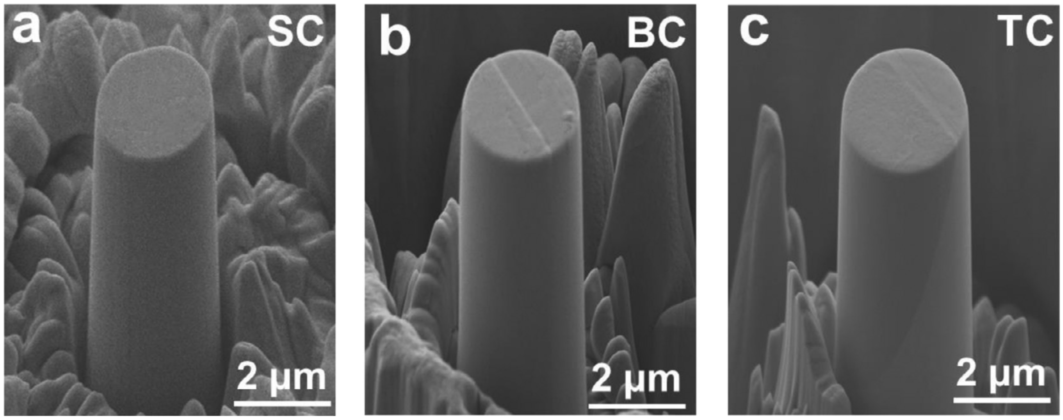

Fig. 2. Representative SEM images of the as-fabricated (a) [111]-oriented SC, (b) BC, and (c) TC pillars, respectively.

exhibited prominent serrations. This made the determination of the yield strength, σ_y, using the 0.2% strain offset method inaccurate [24]. Instead, σ_y values were determined by selecting the point where the elastic stage of deformation ends.

3. Results

3.1. Bulk tensile and compression tests

The overall microstructure of the CoCrFeNi HEA is characterized by EBSD, as shown in Fig. 3(a). The grains are equiaxed and uniformly distributed, where no evident texture can be seen. Annealing twins are found in ~ 90% of the grains. The distribution of different types of boundaries is displayed in Fig. 3(b), where red and green lines mark the HAGBs and TBs, respectively. EBSD measurements reveal that the HEA examined in this work consists of 54.3% ± 4.2% TBs, with the rest being HAGBs; the existence of low-angle grain boundaries (LAGBs) could not be detected. The average grain size (d), considering only HAGBs, was estimated to be 46.2 ± 32.3 μm.

Representative true stress–strain responses measured in uniaxial compression and tension on the PC specimens are shown in Fig. 4(a, b), respectively. In Fig. 4(a), blue, black, and red lines correspond to the tests at $\dot{\varepsilon}$ = 10^{-4}, 10^{-3}, and 10^{-2} s^{-1}, respectively. The flow stress at 10^{-2} s^{-1} is higher than those obtained at 10^{-3} and 10^{-4} s^{-1}. No difference between 10^{-3} and 10^{-4} s^{-1} test results is evident before ~7% true strain. With increasing strain, the effect of strain rate becomes more significant. As seen from the tensile responses displayed in Fig. 4(b), both strength and ductility are strain-rate-dependent. Samples tested at $\dot{\varepsilon}$ = 10^{-2} s^{-1} can reach an ultimate tensile strength (UTS) of ~1000 MPa and ~57% elongation, while those at $\dot{\varepsilon}$ = 10^{-4} s^{-1} exhibit a UTS of ~851 MPa and ~48% elongation. However, the variations in both UTS and ductility will not be pursued further in this study, as the focus is on the effect of $\dot{\varepsilon}$ on σ_y. The double logarithmic plots of σ_y versus $\dot{\varepsilon}$ obtained from both compression and tension tests are shown in Fig. 4(c). A linear increase in log σ_y with log $\dot{\varepsilon}$ is seen, suggesting notable SRS.

3.2. Compression of single crystal micropillars

The maximum values of the Schmid factors, SF_{max}, for [111], [114], and [101] crystal orientations are listed in Table 1, along with the specific slip systems.

Typical morphologies of the deformed SC micropillars at $\dot{\varepsilon}$ =10^{-3} s^{-1} are shown in Fig. 5 along with the schematic illustrations of the corresponding slip systems having SF_{max}. (Micrographs for the rest of the conditions are shown in Fig. S2 of the Supplementary Information.) For all three orientations, planar slip is the predominant deformation mechanism, as evidenced by the slip traces on the surface of the pillars. Comparison of the SEM images and the slip system schematics shows that the directions of the slip traces on the pillars correspond well with the slip systems having SF_{max} (or equivalently, the highest resolved shear stress, RSS). In the [111] SC pillars, there are 6 slip systems which possess SF_{max} of 0.272 on 3 slip planes (see Table 1). The activated slip plane in the [111] pillar (Fig. 5(a)) could be either one of $(\bar{1}11)$, $(1\bar{1}1)$, or $(11\bar{1})$. Similarly, the activated slip planes in [114] pillar (Fig. 5(b)) could be either $(\bar{1}11)$ or $(1\bar{1}1)$. Although there is more than one slip plane with SF_{max}, activation of only one is dominant for most (~80%) in [111] and [114] SC pillars, irrespective of $\dot{\varepsilon}$. For [101] SC pillars, both the possible slip planes, i.e., (111) and $(1\bar{1}1)$, are activated, leading to the formation of the duplex slip traces that are observed in Fig. 5(c). Due to the different values of ϕ (the angle between the loading direction and the normal to the slip plane) in the slip systems that possesses SF_{max} (i.e., 70.5°, 57.0°, and 35.3° for [111], [114], and [101] SC pillars), the morphologies of deformed pillars vary.

Representative engineering stress–engineering strain responses of the [111], [114], and [101] SC pillars, obtained at $\dot{\varepsilon}$ = 10^{-3} and 10^{-2} s^{-1}, are plotted in Fig. 6. (For clarity, the plots obtained at $\dot{\varepsilon}$ = 5 × 10^{-3} are omitted here but are shown in Fig. S3 of the Supplementary Information). For [111] pillars, the mechanical responses under different $\dot{\varepsilon}$ are similar, resulting in the near-overlap of the curves (Fig. 6(a)). Despite the small serrations of stress (also known as stress drops [25]) throughout the plastic deformation region, no significant ones are observed. The work hardening rate is constant throughout the plastic deformation regime. For [114] pillars, the serrations are much more significant than in the [111] ones and the stress even drops to zero in some instances (see Fig. 6(b)). These large stress drops are attributed to the transient stress relief events due to dislocation avalanches [25]. Moreover, as shown in Fig. 6(b), almost no work hardening was observed since these dislocation avalanches can markedly reduce the dislocation density within the samples. While responses to the increased $\dot{\varepsilon}$ can be seen at the yield point, the stress–strain plots obtained at $\dot{\varepsilon}$ = 10^{-3} and 10^{-2} s^{-1} overlap after 2% engineering strain. For [101] pillars, both large stress serrations and slight work hardening were observed (Fig. 6(c)). While the dislocation avalanches are responsible for the large stress drops, the interaction between dislocations causes the strain hardening as multiple slip systems are activated in these pillars (Fig. 5(c)). Similar to that in [114] SC pillars, SRS on yielding is seen.

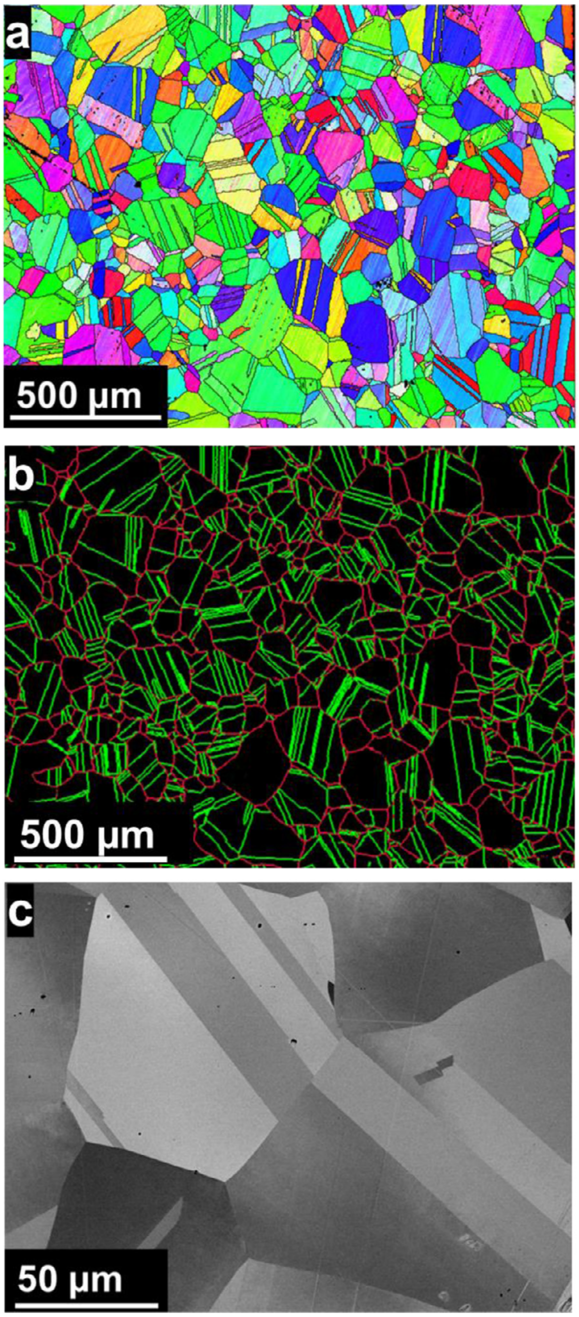

Fig. 3. Representative microstructures of the CoCrFeNi HEA showing (a) an EBSD IPF map, (b) the boundary distribution (where red and green lines represent the high-angle grain boundaries and the twin boundaries, respectively), and (c) a higher magnification BSE image of the microstructure. (For interpretation of the references to color in this figure legend, the reader is referred to the web version of this article).

3.3. Compression of bi- and twined-crystal micropillars

Representative morphologies of the [111] / [114]-oriented BC and TC micropillars after compression at $\dot{\varepsilon} = 10^{-3}$ s^{-1} and the slip systems with SF_{max} in both grains are shown in Fig. 7 (Rest of the images are displayed in Fig. S2 of the Supplementary Information). Despite the same orientation combinations, the deformation behavior of them is distinct. For BC pillars, plastic deformation is carried out by the individual grains (Fig. 7(a)). The fact that the slip traces on either side of the GB are not contiguous indicates that the dislocations could not cut across the GB. Unlike the [111] and [114] SC pillars where activation of single slip plane is predominant, two slip planes are activated in both parts of the BC pillar. In [111] part, these planes are either two among $(\bar{1}11)$, $(1\bar{1}1)$, and $(11\bar{1})$, while in [114] part, $(\bar{1}11)$ or $(1\bar{1}1)$ planes are activated. Regarding the TC pillars (Fig. 7(b)), the observed continuity in the slip traces across TB suggests that the boundary does not arrest or block the dislocation transmission across it. The activated slip planes in [111] part of TC pillars are similar to those in BC pillars. Only one slip plane was found activated in the [114] component of the TC pillar, which could be attributed to the fact that one of the {111} planes is TB itself [26,27].

Mechanical responses of the BC and TC pillars deformed at $\dot{\varepsilon} = 10^{-3}$ and 10^{-2} s^{-1} are plotted in Fig. 8. (Plots obtained at $\dot{\varepsilon} = 5 \times 10^{-3}$ s^{-1} are shown in Fig. S3 of the Supplementary Information). The mechanical responses of BC pillars are similar to those of [111] SC pillars, showing insignificant SRS, evident strain hardening and limited serrations. The TC pillars, in contrast, show σ_y values lower than those of the BC counterparts. After yielding, more pronounced serrations and lower strain hardening were also observed in TC pillars.

Variation of σ_y in the examined pillars is plotted as a function of the strain rate in Fig. 9. The following three features are noteworthy: 1) While [101] and [114] SC pillars and TC pillars exhibit SRS, σ_y of [111] SC pillars and BC pillars are insensitive to the strain rates (within the range examined). 2) Among the SC pillars, σ_y is clearly orientation dependent, with [111] and [101] pillars having the maximum and minimum σ_y values, respectively. 3) σ_y values of BC pillars are like (or slightly lower than) those of the [111] SC pillars, whereas σ_y of TC pillars is between those of the [111] and [114] SC pillars.

4. Discussion

4.1. Strength and plastic deformation of micropillars

To understand the rate-sensitive deformation mechanism in the HEA observed during the micropillar compression tests, yielding and plastic deformation mechanisms in such micron-sized samples need to be understood first. The following unique characteristics, which are typically associated with micron-scale pillar compression test results, were also found in the present study. (1) Size dependence of yield strength, with higher strength observed as the sample volume gets smaller [28–30]. (2) Intermittent stress drops (or strain bursts) that are stochastic in nature [31]. (3) Relatively high SRS as compared to that observed in bulk samples [32,33]. All these features are often attributed to the dominance of the source-controlled deformation mechanisms [34,35].

4.1.1. Single-crystals

In bulk materials, critical RSS (CRSS) is predominantly determined by the stress required to activate the dislocation sources in a given slip system, which are typically double-pinned Frank-Read sources [36]. With their interactions with free surfaces in micron-scale samples, these double-pinned dislocation sources are truncated into single-arm ones. When the sample dimension is further reduced to tens of nanometers or less, dislocation starvation [35] and surface nucleation [37] become predominant mechanisms. Such size effect is also captured here: the values of CRSS, obtained from macroscale compression tests of [110]- and [111]-oriented SC CoCrFeNi samples were reported to be 43 and 39 MPa, respectively [38], which are significantly lower than the CRSS estimated through the micropillar compression experiments of the present study (~175 MPa). This is also in agreement with the inverse power-law dependence of yield strength, and thus CRSS, on the pillar size [39].

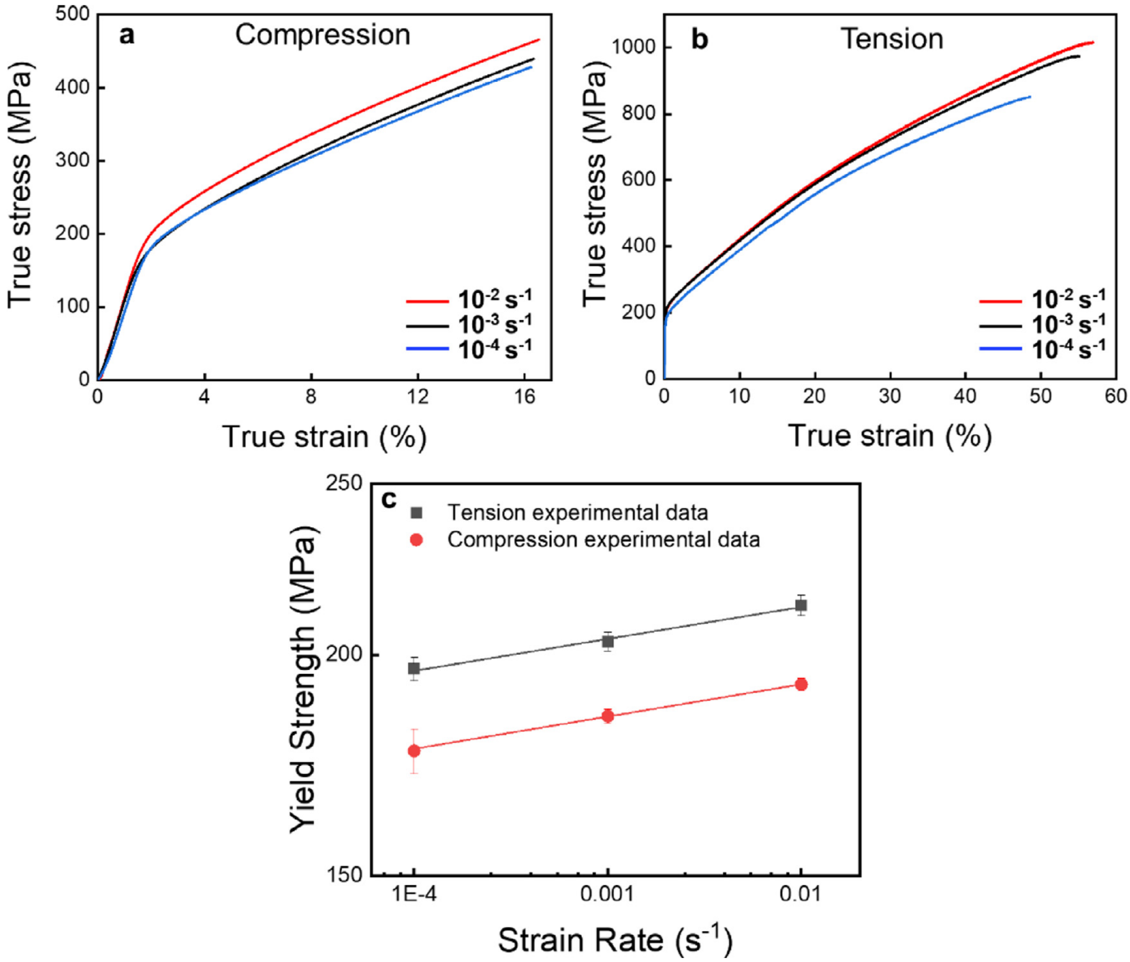

Fig. 4. Representative true stress–true strain responses obtained from the uniaxial (a) compression and (b) tension tests on the PC specimens. (c) Double logarithmic plots of the yield strength versus strain rate for both compression and tension tests. The lines mark the linear fits of the double logarithmic plots. (For interpretation of the references to color in this figure, the reader is referred to the web version of this article).

Table 1
Maximum Schmid factors and corresponding slip systems for the CoCrFeNi HEA micropillars having different orientation.

Orientation	Max. Schmid Factor, SF_{max}	Corresponding Slip Systems
[111]	0.272	$(\bar{1}11)[110]$, $(\bar{1}11)[101]$, $(1\bar{1}1)[110]$, $(1\bar{1}1)[011]$, $(11\bar{1})[101]$, $(11\bar{1})[011]$
[114]	0.453	$(\bar{1}11)[101]$, $(1\bar{1}1)[011]$
[101]	0.408	$(111)[\bar{1}10]$, $(111)[0\bar{1}1]$, $(1\bar{1}1)[110]$, $(1\bar{1}1)[011]$

Table 2
Average values of the work hardening rates and magnitudes of the observed stress drops in different micropillars.

	Strain rate (s^{-1})	SC			BC	TC
		[111]	[114]	[101]		
Work hardening rate (GPa)	10^{-3}	5.4 ± 0.4	0.2 ± 0.02	3.2 ± 0.4	5.7 ± 0.5	2.3 ± 0.4
	10^{-2}	4.8 ± 0.6	0.07 ± 0.03	2.5 ± 0.4	4.9 ± 0.5	2.2 ± 0.2
Stress drop (MPa)	10^{-3}	18.7 ± 7.9	118.9 ± 32.1	60.4 ± 30.0	10.2 ± 2.3	61.3 ± 14.8
	10^{-2}	11.6 ± 6.9	78.2 ± 55.8	51.9 ± 31.5	8.5 ± 1.9	55.8 ± 16.9

As deformation proceeds, characteristic stress drops occur, which are generally observed in all SC, BC, and TC micropillars to varying degrees (see Figs. 6 and 8). Such stress drops are believed to be associated with the avalanches of dislocation nucleation and glide towards the sample surface for eventual escape. The variations in the magnitudes of the stress drops are also closely related to the strain hardening behavior. Average strain hardening rates and magnitudes of the stress drops, obtained within 2% and 4% engineering strain window, are listed in Table 2. (The choice of 2 and 4% as the limits for estimating the hardening behavior is made by recognizing that 2% engineering strain is the cutoff for all the pillars to yield and that possible taper-induced stress gradient and plastic instability may affect the results at strains higher than 4% [40]). A quantitative comparison of the stress drop magnitudes (Figs. 6 and 8) indicates that they are inversely related to the work hardening rate (Fig. 10). The following is the rationale for this observation. Typically, strain hardening should be absent in a SC FCC micropillar when only single slip system is activated [41]. The stochastic stress drops (or strain burst) commonly seen in these pillars are characteristics of either dislocation escaping

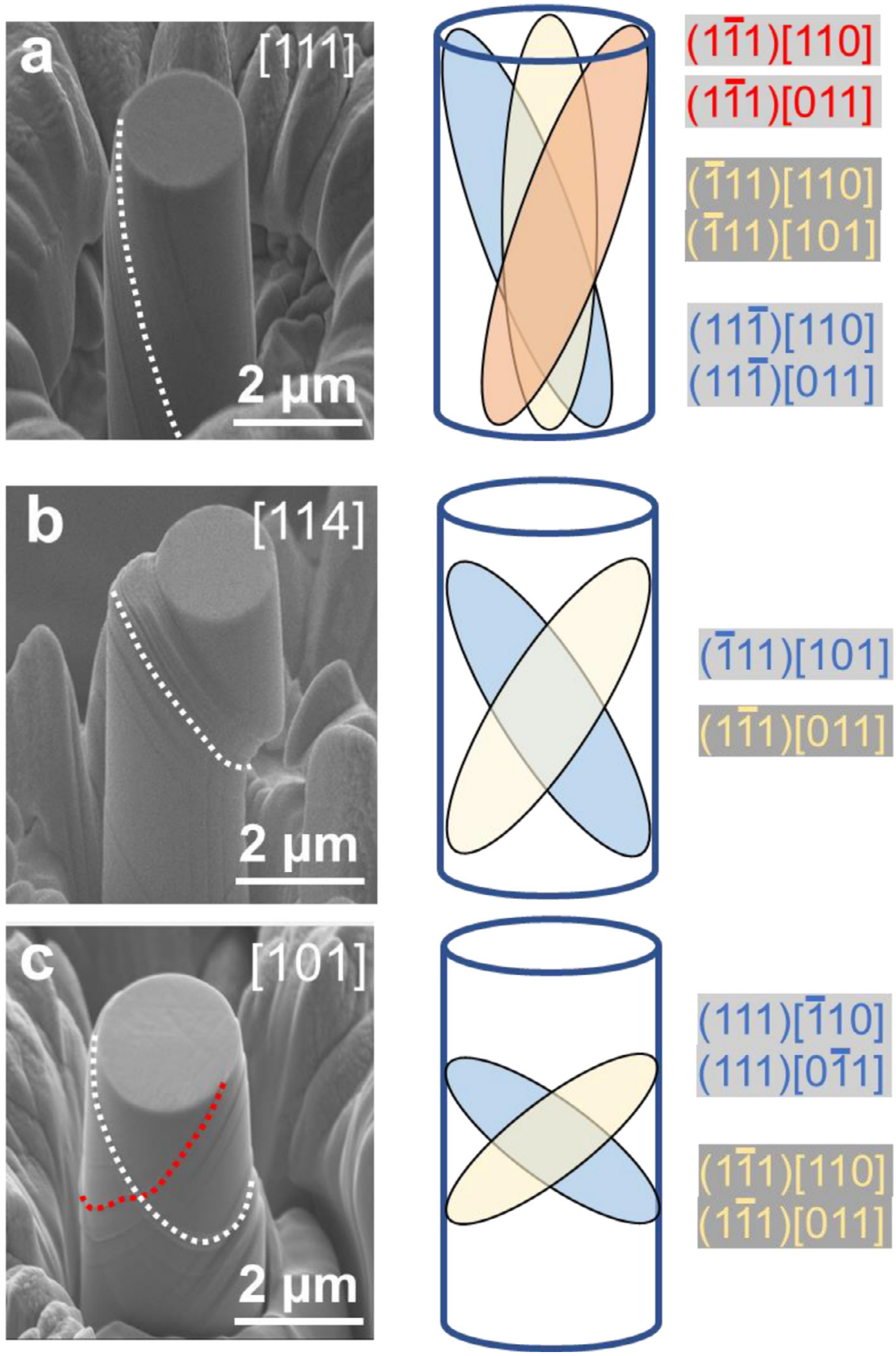

Fig. 5. Morphologies of the compressed SC pillars, characterized by SEM and schematics of the slip systems with the maximum Schmid factors, SF_{max}. (a) [111], (b) [114], and (c) [101] oriented pillars deformed at $\dot{\varepsilon} = 10^{-3}$ s^{-1}.

from surface or due to dynamic reconstruction of jammed dislocation sub-structures [37,41]. In either case, this results in a decrease in dislocation density within the pillar that, in turn, leads to a work hardening rate close to 0 due to the limited interactions between dislocations; for instance, no work hardening was observed in [100]-oriented Cu and CoCrFeNi HEA SC pillars in which large stress drops were present [16,41].

On the basis of the above discussion and the deformation morphology observed in Fig. 5, the plastic deformation behavior of SC pillars can be rationalized as following. In the [114] SC pillars, the high-magnitude stress serrations and nearly no work hardening characteristics agree well with the deformation morphology in Fig. 5(b), where no barrier of dislocation motion was seen. In the [111] SC pillars (Fig. 5(a)), on the contrary, the serrations in the stress-strain responses are not pronounced. They mostly manifest as small and continuous stress drops. Consequently, work hardening is evident. This is due to a higher ϕ that effects the deformation in the following two ways. (1) A higher ϕ makes the distance for dislocations to travel to the pillar surface large. (2) As the slip planes intersect with the bottom of the pillars, dislocations can get accumulated—instead of escaping from the surface [34,37,41]. Both these factors favor dislocation multiplication that reduces the magnitude of the serrations while enhancing the work hardening. In [101] SC pillar (Fig. 5(c)), even though dislocations can still escape from the surface, the stress drop extent is only intermediate, inducing mild strain hardening, which is most likely a result of the

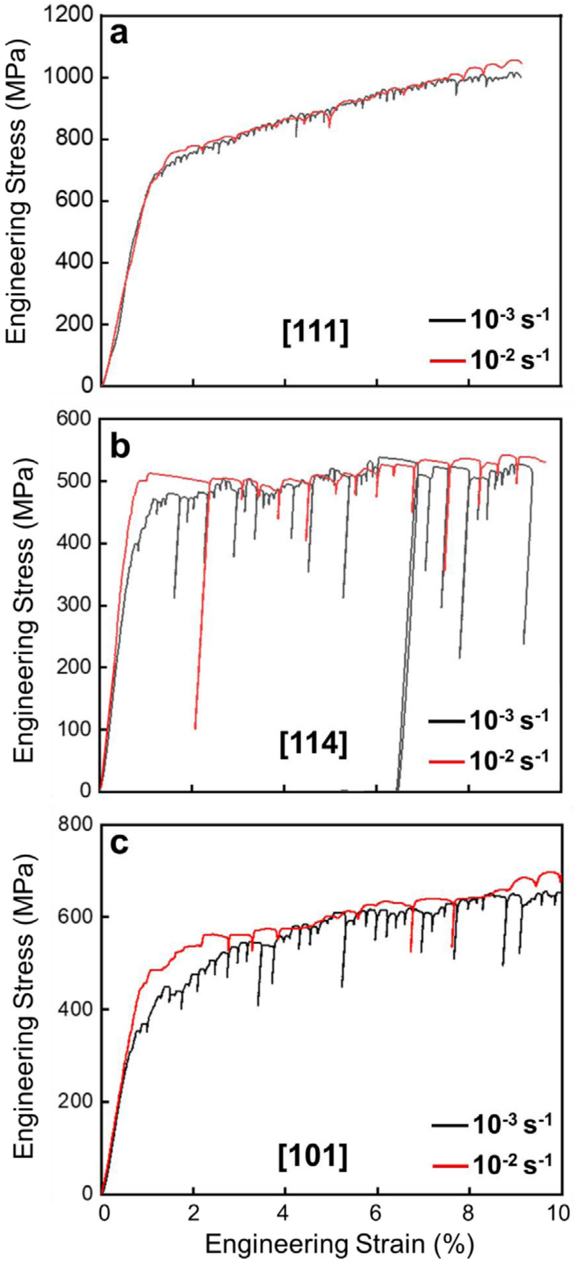

Fig. 6. Representative engineering stress-strain responses of (a) [111], (b) [114], and (c) [101] SC micropillars subjected to uniaxial compression at 10^{-2} and 10^{-3} s^{-1} strain rates.

dislocation interactions initiated by the activations of multiple slip systems.

4.1.2. Bi- and twinned-crystals

Next, we discuss the roles of HAGBs and TBs in the deformation behavior of micropillars. As seen from Fig. 8, despite the same orientation combinations ([111] and [114]), the effect of HAGB and TB on the dislocation motion is distinct. Specifically, the mechanical responses of BC pillars are closer to that of the harder component (the [111]-oriented grain), marked by the high work hardening rate and muted serrations (Fig. 10). The TC pillars, on the other hand, exhibit moderate work hardening and pronounced stress drops (Fig. 10). All these features reflect the 'average' of the two crystallographic components that make the pillars up. In Fig. 7, the first noticeable feature is that often two slip planes are activated in both parts of the BC and TC pillars, which is unlike the [111] and [114] SC pillars where single slip plane prevails. The existence of the interface (GB or TB) effectively reduces the dislocation mean free path. Hence, it reduces the influence of the relatively large ϕ on restricting secondary slip system. Irrespective of the number of activated slip planes in each constituent, the dislocations in the 'soft' grain ([114], with the larger SF_{max}) would always be the first to get activated upon loading. Their motion would then be affected by the interface, either HAGB or TB. Such interaction between interface and moving dislocations dominates the deformation behavior of the pillars [42].

Unlike the well-established GB mediated strengthening mechanism in bulk polycrystalline materials (captured by the Hall-Petch relationship), disparate effects have been reported for a single GB in micropillars [43,44]. More specifically, it is found that Al bi-crystal micropillars show higher strength, stronger hardening, and less serrated flow due to the dislocation pile-up against GB [43]. Yet, others reported that GB in Al bi-crystal pillars acts as a sink of dislocations by absorbing them, resulting in near-invariance in strength, lower hardenability, and larger strain serrations [44]. Despite the divergence, it is reasonable to expect that HAGB is difficult for dislocations to penetrate through [45]. In the BC pillar, it is observed that HAGB acts as a strong barrier for dislocation motion, as evidenced by the discontinuity of the slip traces across HAGB (Fig. 7(a)). Upon loading, the single-arm dislocation source in the soft grain ([114], with larger SF_{max}) would be activated first. However, these dislocations cannot transmit through HAGB (Fig. 11). For compatibility, plasticity in the 'hard' grain ([111], with smaller SF_{max}) requires the activation of the dislocations inside it as well, which can only happen when CRSS (or σ_y) of the [111]-oriented grain is attained. As a result, σ_y of the BC pillar is similar to (slightly lower) that of the [111] SC pillar. Such a slight difference in σ_y can be attributed to the different deformation mechanism between [111] part of the BC pillar and [111] SC pillar (Figs. 5 and 7).

Compared to GB, effect of a single TB in micropillars is markedly different. In recent studies, it was reported that Cu micropillars containing coherent TBs do not show any noticeable difference in mechanical response [46,47]. It is also observed that vast majority of dislocations can transmit across TB and leave connected slip traces in both grains [46,47]. In the TC pillar, the dislocations that emanate from the soft component ([114]) can transmit across the coherent boundary (Fig. 11) and facilitate the deformation of the hard component ([111]), as indicated by the contiguous slip traces across the TB (Fig. 7(b)). Such accommodation of the deformation by the hard part of the pillar containing TB leads to a lower σ_y than that of the [111] SC pillar. As seen from Fig. 9, σ_y of TC pillar is in between those of [111] and [114] SC pillars. It is worth noting that the plastic deformation in BC and TC pillars is governed by the interface and its interaction with dislocations, rather than dislocation gliding within respective grains. Therefore, the effect of non-uniform volume fraction of the two constituents in TC pillars (i.e., the TB inclined to, instead of normal to, the sample surface, as observed in Fig. 7(b)), if any, can be neglected.

4.2. Dislocation activation parameters

To gain more insights into the plastic deformation mechanisms, the rate-dependent, thermally-activated deformation parameters, viz. the SRS parameter, m, and the activation volume, V^*, were estimated. From the double logarithmic plots of σ_y and $\dot{\varepsilon}$ displayed in Figs. 4 and 9, values of m in bulk tension, compression, and micropillar compression were obtained and are listed in Table 3.

For coarse grained pure metals with FCC crystal structure (e.g., Cu and Ni), SRS is typically insignificant (m < 0.01) [14,17,48]. In contrast, markedly higher m values are reported for FCC HEAs, irrespective of the testing technique employed [8,49,50]. The values of

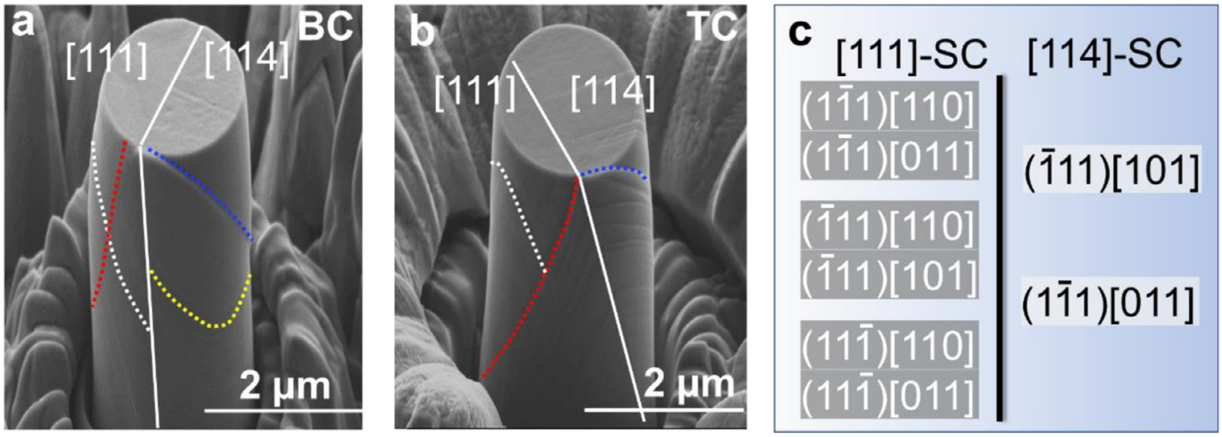

Fig. 7. Morphologies of the compressed (at $\dot{\varepsilon} = 10^{-3}$ s^{-1}) (a) BC and (b) TC micropillars, with (c) the corresponding list of the activated slip systems in both the pillars.

Table 3
List of the SRS exponent m and activation volume V^* values in this study.

	Bulk Tension	Bulk Compression	[111] SC pillar	[114] SC pillar	[101] SC pillar	BC pillar	TC pillar
m	0.018	0.019	0	0.052	0.048	0	0.025
V^* (in b^3)	163.3	181.5	N.A.	41.9	35.4	N.A.	43.2

$m = 0.018$ and 0.019 obtained using bulk tension and compression testing, respectively, agree well with the typical values reported in coarse grained FCC HEAs (~0.012–0.02) [20,51,52]. Such difference in m between pure metals and HEAs has been proposed to be caused by the Labusch-type strengthening mechanism in the latter, where unique structural features of HEA (such as lattice and modulus mismatch and short-range ordering) play important roles [17]. Note that despite consistent tension-compression asymmetry in σ_y, the difference in m value is insignificant. For SC pillars, an evident orientation dependence can be seen; [111] pillar did not show a clear SRS while the m values of [114] and [101] pillars are much larger than that in bulk. Such higher m of pillars is also reported in the literature [16,53].

Another important parameter linking the rate-sensitive deformation with the plastic deformation mechanism is V^* [12], which is given by:

$$V^* = \sqrt{3}kT\left(\frac{\partial \ln\dot{\varepsilon}}{\partial \sigma_y}\right), \tag{3}$$

where k and T are Boltzmann's constant and absolute temperature, respectively. Typically, values of V^* are expressed in terms of b^3 ($b = \sim$0.225 nm for CoCrFeNi [8,17]). They are listed in Table 3. It is well established that the magnitude of V^* can be used to identify different deformation mechanisms in bulk or small-volume metals [8,12,54]. For instance, V^* ranging between ~100 and 1000b^3 was reported for forest dislocation cutting mechanism in CG FCC metals. Since the V^* values obtained from the macroscale tests are within this range, it is reasonable to conclude that the forest dislocation mechanism controls the plasticity in them. Values of V^* for the single-arm dislocation source mechanism, which dominates the plastic deformation in the micropillars, ranges from tens to hundreds of b^3. In contrast, the surface dislocation nucleation mechanism (as in nano-pillars) generally results in V^* of less than ~10b^3 [32,55]. A transition between these two mechanism may occur with the change in sample size [55,56]. Since the plastic deformation in the [111] SC pillars and the BC pillars is rate insensitive, V^* could not be obtained for them. V^* in all the other micropillar tests range between ~35 and 43b^3, confirming that the single-arm source mechanism is responsible for the plastic flow initiation in these micropillars. Consequently, a dynamic balance between the dislocation nucleation and escape from the pillar surfaces can be envisioned, and a surge of dislocation density can occur when $\dot{\varepsilon}$ is increased suddenly, caused by the dislocation nucleation rate outweighing the loss rate [57]. Due to the increased dislocation density within the sample, the interaction between them is bound to be enhanced, resulting in the increased strength. Therefore, SRS stems from the instantaneous surge of dislocation density, or dislocation multiplication, which is dynamically controlled by $\dot{\varepsilon}$ [58].

The orientation dependency of SRS in SC pillars is rationalized by recourse to the theory that single-arms revolve on the corresponding slip planes as the plastic deformation progresses [59]. The dynamic changes of single-arm source mediated dislocation density in the [111], [114] and [101] SC pillars are schematically illustrated in Fig. 12. As seen from them, irrespective of the orientation, an instantaneous increase in the dislocation density with $\dot{\varepsilon}$ can be envisioned. However, the orientations of slip planes and pillar geometry can exert the influence on the interactions between the single-armed dislocation spirals, resulting in the orientation dependency of SRS. More specifically, due to the large ϕ (70.5°) in the [111] SC pillars, the slip plane extends into the pillar matrix instead of stopping at the pillar surfaces (Fig. 5(a)). Therefore, the spiraling single-arm dislocations are likely to be impeded at the root of the [111] SC pillar (Fig. 5(a)) [34,41]. As a result, dislocations would pile up at the base and fewer dislocations can escape from the surface, reflected by an increase in the work hardening and the absence of large serrations in the loading curve (Fig. 6(a)). Due to such pile-up of dislocations, the interaction between the gliding dislocations would be weakened, resulting in the insensitivity to $\dot{\varepsilon}$ observed.

In the [114] SC pillars, the number of obstacles for dislocation motion is limited, which manifests as distinct slip-induced shear offsets that can be seen on the pillar surface in Fig. 5(b). Moreover, large stress drops are commonly observed in the stress-strain responses (Fig. 6(b)), indicating that dislocations can readily escape from the surface. In this scenario, interaction between the dislocations at a higher $\dot{\varepsilon}$ play a more prominent role (Fig. 12), leading to an increased m. A different dislocation slip mode, viz. duplex slip, was found in the [101] SC pillars, compared to [111] and [114] ones (shown in Fig. 5(c)) that are dominated by single slip. In the former case, dislocations can escape from the surface and

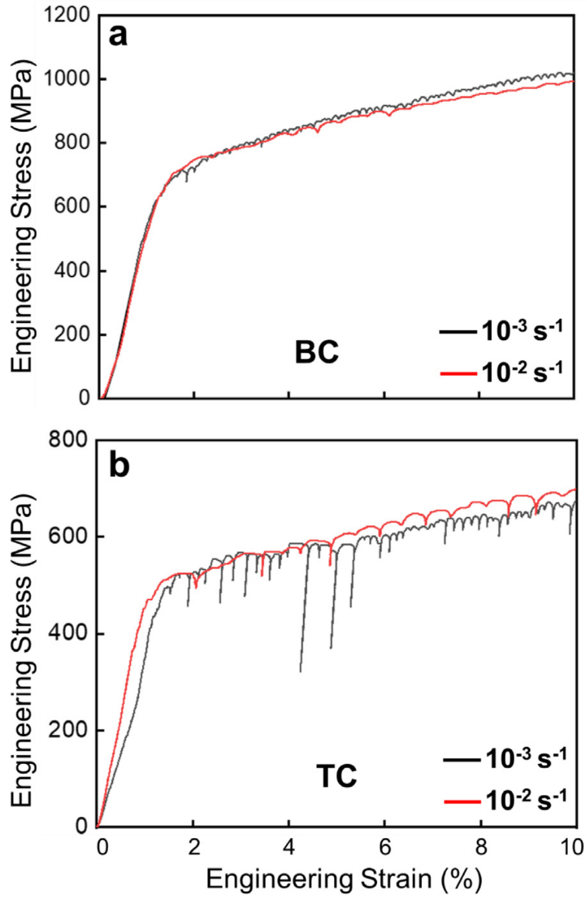

Fig. 8. Representative engineering stress–strain responses of (a) BC and (b) TC micropillars subjected to uniaxial compression at 10^{-2} and 10^{-3} s^{-1} strain rates.

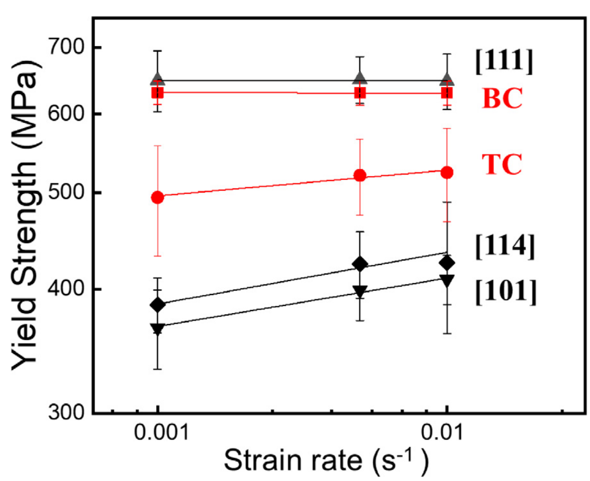

Fig. 9. Double logarithmic plots of yield strength versus logarithmic strain rate for different micropillars tested in this work: [111], [114], [101] SC pillars and [111] / [114] BC and TC pillars.

interact with dislocations on the other slip planes as well. This behavior is reflected in the stress–strain responses (Fig. 6(c)) where dislocation-escape-induced serrations and work hardening exist simultaneously. Therefore, the relatively high m value obtained for the [101] SC pillars (nearly identical as the one for the [114] pillar) can be construed as due to the strong interactions between the gliding dislocations.

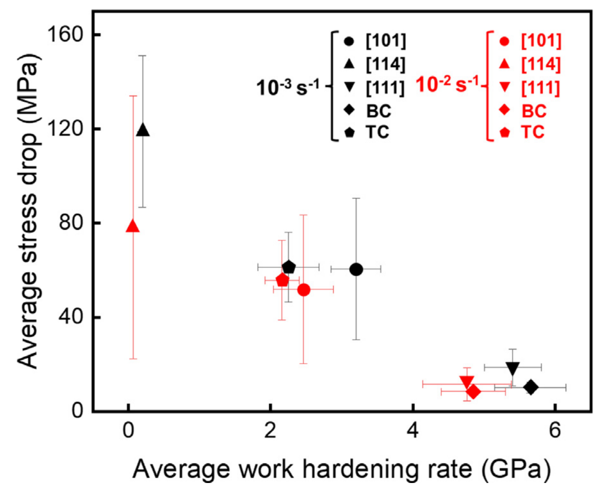

Fig. 10. Variation of the average stress drop magnitude with the average work hardening rate at the strain rates of 10^{-2} and 10^{-3} s^{-1} for different micropillars tested in this work: [111], [114], [101] SC pillars and [111]/[114] BC and TC pillars.

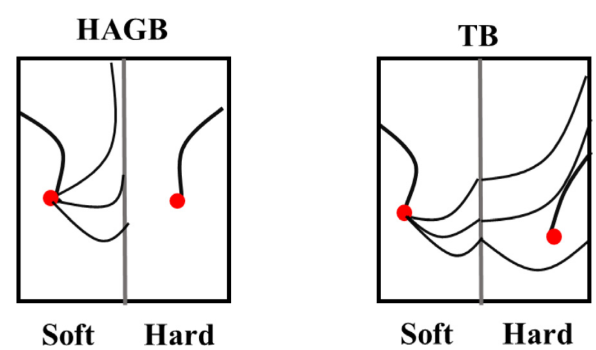

Fig. 11. Schematic illustrations of the effects of high-angle grain boundary (HAGB) and twin boundary (TB) on the dislocation motion.

4.3. Effects of grain and twin boundaries on the strain-rate sensitivity of bi-, twinned-, and poly-crystals

Based on the discussion in Section 4.1.2 and keeping in mind that the barriers for dislocation mobility control SRS, the effect of HAGB and TB on the SRS of BC and TC pillars can be understood. Due to the strong blocking effect of HAGB, the pile up of dislocations would mitigate the SRS of the BC pillar, resulting in $m \sim 0$. This agrees well with the notion that HAGBs are long-range athermal barriers to dislocation motion and thus have insignificant sensitivity in response to either strain rate or temperature [60,61]. Regarding TBs, in spite of the fact that they can permit dislocation transmission, they are not entirely 'transparent' to dislocation motion. Therefore, the SRS of TC pillar is not as evident as [114] SC pillar (Table 3). On the basis of above results and discussion, the effects of HAGBs and annealing TBs on the SRS of bulk CoCrFeNi HEA can be summarized as follows. No SRS can be seen when dislocation pile-up occurs (typically at HAGB), implying HAGB plays insignificant role in SRS, at least in CG metals and alloys. Widespread annealing twins in the current HEA can affect the level of SRS through impeding the dislocation motion without causing significant pile-up.

The effect of GBs on the mechanical behavior of bulk polycrystalline metals and alloys is well known [62]. Apart from the strength, GBs also influence the SRS of bulk materials in a certain regime of d. For illustration, literature values of m of pure Ni are plotted against d in Fig. 13 [10–13,17,63]. As seen from it, m remains nearly constant ~0.004 for d ranging between ~100 nm and

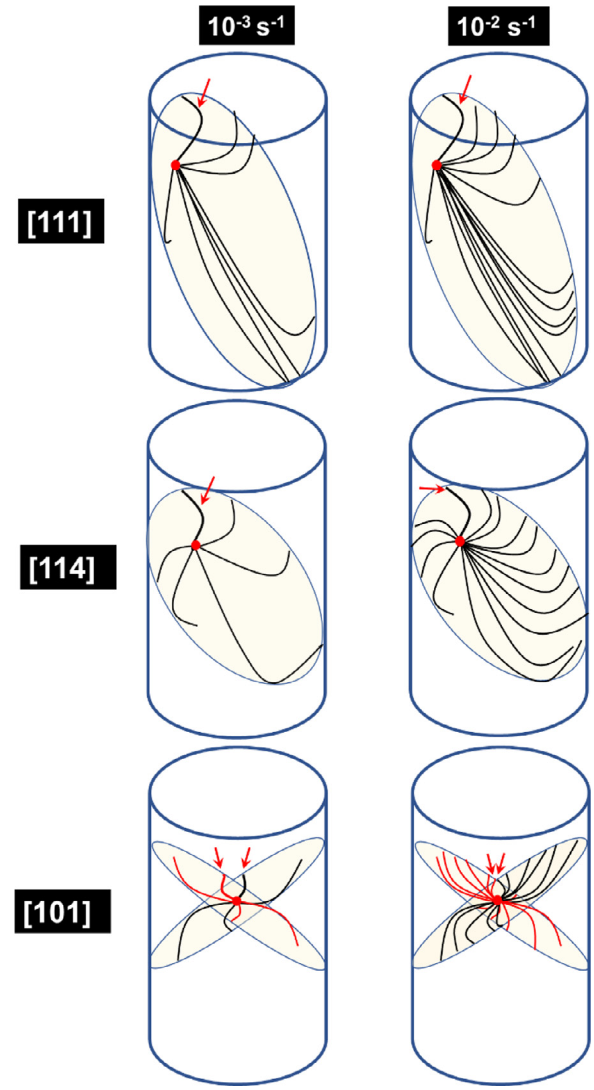

Fig. 12. Schematic illustrations of the dislocation density evolution at 10^{-3} and 10^{-2} s^{-1} strain rates in the [111], [114], and [101] SC pillars. Red dots represent the dislocation pinning points and red arrows point out the single-arm dislocation source. (For interpretation of the references to color in this figure, the reader is referred to the web version of this article).

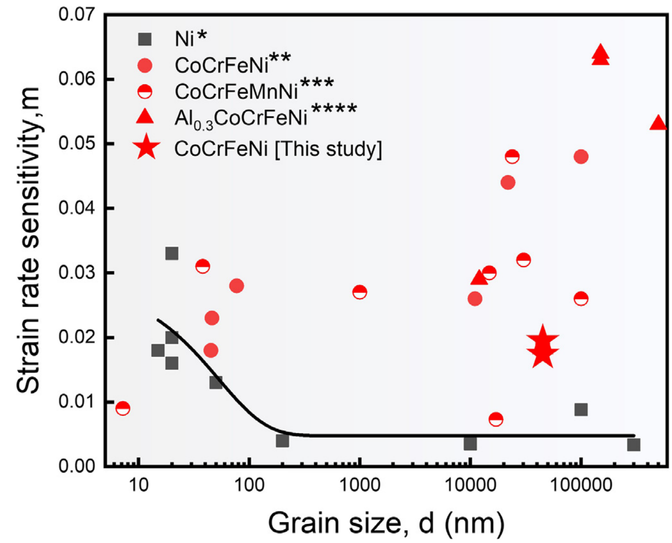

Fig. 13. Variations of the strain-rate sensitivity (m) and grain size (d). Literature data for pure *Ni [10–13,17,63], along with **CoCrFeNi [8,15,17,67], ***CoCrFeMnNi [15,17,19,22,70], and ****$Al_{0.3}$CoCrFeNi HEAs [18,68,69].

~300 μm, i.e., micron to sub-micron regimes. As d approaches nm-regime (below 100 nm), a significant increase in m is noted. Similar trend has also been reported for Cu and its alloys [14,64]. Such a marked increase in m of NC FCC metals was attributed to GB-mediated dislocation activity (dislocation nucleation and/or dislocation depinning at GBs) [10,65,66]. In CG materials, it is known that GBs offer long-range athermal barriers to dislocation motion, which is insensitive to either strain rate or temperature [60]. This may be the reason why m is insensitive to d in CG regime (d > 100 nm).

The variations of m with d for FCC HEAs [8,15,17,18,67–69] are evidently different from those of pure FCC metals (e.g., Cu [14] and Ni [10]), as seen in Fig. 13. First, m of CG FCC HEAs is much higher than that in CG pure Ni, which is believed to be induced by Labusch-type solid solution strengthening in HEAs [17]. Unlike the case for Ni or its alloys [8], where a clear trend in m versus d is found, the m values of CG HEAs are highly diverse (Fig. 13). Although some researchers claimed an inverse d dependency of m in CoCrFeMnNi [19] and $Al_{0.3}$CoCrFeNi [68] HEAs, the large scatter in data of various studies, as seen from Fig. 13, does not appear to support such a conclusion. Through the observations in this study, it is found that plastic behavior of FCC HEAs is not fundamentally different from pure FCC metals; yet their m vs. d relationships are disparate. Based on our experimental results, especially the SRS in SC, BC, and TC pillars, it appears that the role of annealing twins in the SRS of HEAs, which appears to have been overlooked in most of the past studies, requires special attention.

Annealing twins are seldom present in typical pure Cu and Ni, which were examined *a priori*, since they possess relatively high SFEs (Ni ~150 mJ/m^2 and Cu ~80 mJ/m^2 [71]. Thermomechanical processing that may induce twin formation was usually not applied. The FCC HEAs, in contrast, possess much lower SFEs (~20–32.5 mJ/m^2 for the HEAs represented in Fig. 13 [4,23,72]). Moreover, they are often processed by cold working followed by annealing treatment, both of which promote the formation of annealing twins. From the results in this study, it is observed that TC and BC pillars show distinct response at different $\dot{\varepsilon}$. As these annealing twins take up ~54.3% of the total boundaries in the CoCrFeNi HEA examined in the present work, it is reasonable to assume that they play a non-negligible role in the overall SRS of the material. It is also worth noting here that the predominant deformation mechanism in bulk polycrystals of CoCrFeNi HEAs is dislocation slip, rather than deformation twinning, as evidenced by the continuous reduction in the work hardening rate with true plastic strain (see Fig. S4 of the Supplementary Information) [73,74] and the fact that the plastic deformation of CoCrFeNi HEA is characterized by planar slip [4]. Quantification of the annealing twin fraction in the HEAs of literature was not performed, despite the fact that nearly all the HEAs studied consist of wide-spread annealing twins [85]. Hence, it is difficult to ascertain the relationship between twin fraction and SRS. Nevertheless, based on the current results and the prior observation that nano-scale twinning causes remarkable enhancement in SRS [67,75], it appears reasonable to assume that one of the possible reasons for the large diversity in SRS values of CG FCC HEAs may be the varying degrees of annealing twins in the examined samples. Therefore, a systematic study on the rate-sensitive deformation behavior of FCC HEAs with various fractions of annealing twins will be of critical significance to build up a thorough understanding on the issue.

Before closing, it is constructive to discuss about the differences and (possible) connections between the rate-sensitivities of bulk and micro-scale sample. It is well documented that the rate-limiting, thermally activated deformation mechanism in the uniaxial tension and compression tests of coarse grained polycrystalline samples of FCC metals and alloys is forest dislocation cutting [12,54]. This mechanism is controlled by the features that dictate dislocation mobility such as the formation of jogs on intersection of dislocations or the recombination of short attractive junctions [54]. In the small-scale mechanical tests on the samples with limited material volumes (for instance, micropillars in the present study), the rate limiting mechanism would be dislocation nucleation, from either the truncated single-arm sources (in micropillars) or free surfaces (in nanopillars). As a result, the thermal activation parameters, viz. m and V^*, obtained from macro- and micro-scale tests may not be directly applicable to rationalize those of the bulk. Specifically, in the current work, the bulk tests give m of $\sim$0.018 and V^* of the order of 10^2b^3, whereas micropillar compression tests show different m (ranging from 0 to 0.052) and V^* in the order of 10^1b^3 (for the cases where a value could be obtained). Nevertheless, small-scale mechanical tests such as micropillar tests do have some advantages in revealing the mechanical responses of interfaces (in the current case, BC and TC), which provide valuable insights for a better understanding of the fundamental plastic deformation processes [76–79]. Such an understanding offers promising ways of tailoring mechanical properties of bulk materials through purposely manipulating the fraction and distribution of interfaces (e.g., GBs, TBs) [80–82]. More specially, given the findings that TBs and GBs exert distinct influence on the rate-limiting, thermally activated deformation, and that their existence can be readily adjusted by thermomechanical processing (e.g., rolling, annealing), SRS and the related the mechanical behavior of FCC HEAs can therefore be microstructurally engineered.

5. Summary

Micropillar compression tests on SC, BC, and TC pillars along with bulk uniaxial tension and compression tests are investigated to examine SRS as well as the effects of different microstructural interfaces on the plastic deformation response of an FCC CoCrFeNi HEA. Characterization of the SC pillars after compression shows that the plastic deformation (yield strength, stress drops, strain hardening, and SRS) of HEA micropillars is indeed controlled by the Schmid law that depends on the geometry of the slip planes in different SC pillars. Pillar compression test results and deformation morphology characterization of the BC and TC pillars that share the same component grains reveal distinct effects of these interfaces on the plastic deformation. While GBs are impregnable to dislocations, TBs allow for dislocation transmission from soft [114]-to hard [111]-oriented grains, resulting in a negligible effect from GBs while accommodating ('averaging') effect from TB on the SRS. Based on these results and the fact that annealing TBs widely exist in FCC HEAs, we conclude that a large diversity in the reported SRS values of FCC HEAs could be due to the presence of annealing twins to varying degrees in the investigated samples.

Acknowledgments

This work at Nanyang Technological University was supported by Agency for Science, Technology and Research (A*STAR) of Singapore via the Structural Metal Alloys Programme (No. A18B1b0061). The work at Hanyang University was supported by the NRF grants (Nos. 2020R1A2B5B01001446 and 2020R1A5A6017701).

Supplementary materials

Supplementary material associated with this article can be found, in the online version, at doi:10.1016/j.jmst.2021.12.025.

References

[1] B. Cantor, I. Chang, P. Knight, A. Vincent, Mater. Sci. Eng. A 375 (2004) 213–218.
[2] Y. Zhao, D.H. Lee, M.Y. Seok, J.A. Lee, M. Phaniraj, J.Y. Suh, H.Y. Ha, J.Y. Kim, U. Ramamurty, J.I. Jang, Scr. Mater. 135 (2017) 54–58.
[3] Y. Chen, Y. Fang, X. Fu, Y. Lu, S. Chen, H. Bei, Q. Yu, J. Mater. Sci. Technol. 73 (2021) 101–107.
[4] Y. Wang, B. Liu, K. Yan, M. Wang, S. Kabra, Y.L. Chiu, D. Dye, P.D. Lee, Y. Liu, B. Cai, Acta Mater. 154 (2018) 79–89.
[5] S. Yoshida, T. Bhattacharjee, Y. Bai, N. Tsuji, Scr. Mater. 134 (2017) 33–36.
[6] F. Otto, A. Dlouhý, C. Somsen, H. Bei, G. Eggeler, E.P. George, Acta Mater. 61 (2013) 5743–5755.
[7] Z. Wu, H. Bei, G.M. Pharr, E.P. George, Acta Mater. 81 (2014) 428–441.
[8] Y. Zhao, X. Wang, T. Cao, J.K. Han, M. Kawasaki, J.I. Jang, H.N. Han, U. Ramamurty, L. Wang, Y. Xue, Mater. Sci. Eng. A 782 (2020).
[9] Y. Zhao, J.M. Park, D.H. Lee, E.J. Song, J.Y. Suh, U. Ramamurty, J.I. Jang, Scr. Mater. 168 (2019) 76–80.
[10] C.D. Gu, J.S. Lian, Q. Jiang, W.T. Zheng, J. Phys. D Appl. Phys. 40 (2007) 7440–7446.
[11] R. Schwaiger, B. Moser, M. Dao, N. Chollacoop, S. Suresh, Acta Mater. 51 (2003) 5159–5172.
[12] Y. Wang, A. Hamza, E. Ma, Acta Mater. 54 (2006) 2715–2726.
[13] F. Dalla Torre, H. Van Swygenhoven, M. Victoria, Acta Mater. 50 (2002) 3957–3970.
[14] J. Chen, L. Lu, K. Lu, Scr. Mater. 54 (2006) 1913–1918.
[15] M. Shabani, J. Indeck, K. Hazeli, P.D. Jablonski, G.J. Pataky, J. Mater. Eng. Perform. 28 (2019) 4348–4356.
[16] Y. Xiao, Y. Zou, A.S. Sologubenko, R. Spolenak, J.M. Wheeler, Mater. Des. 193 (2020).
[17] Z. Wu, Y. Gao, H. Bei, Acta Mater. 120 (2016) 108–119.
[18] S. Gangireddy, B. Gwalani, K. Liu, R. Banerjee, R.S. Mishra, Mater. Sci. Eng. A 734 (2018) 42–50.
[19] L. Xiao, P. Huang, F. Wang, J. Mater. Sci. Technol. 86 (2021) 251–259.
[20] M. Komarasamy, N. Kumar, R.S. Mishra, P.K. Liaw, Mater. Sci. Eng. A 654 (2016) 256–263.
[21] Z. Han, W. Ren, J. Yang, Y. Du, R. Wei, C. Zhang, Y. Chen, G. Zhang, J. Alloy. Compd. 791 (2019) 962–970.
[22] G. Laplanche, J. Bonneville, C. Varvenne, W. Curtin, E.P. George, Acta Mater. 143 (2018) 257–264.
[23] G.D. Sathiaraj, P.P. Bhattacharjee, J. Alloy. Compd. 637 (2015) 267–276.
[24] J. Zhang, K. Kishida, H. Inui, Int. J. Plast. 92 (2017) 45–56.
[25] F.F. Csikor, C. Motz, D. Weygand, M. Zaiser, S. Zapperi, Science 318 (2007) 251–254.
[26] Q. Huang, Q. Zhu, Y. Chen, M. Gong, J. Li, Z. Zhang, W. Yang, J. Wang, H. Zhou, J. Wang, Nat. Commun. 12 (2021) 6695.
[27] Y.T. Zhu, X.Z. Liao, X.L. Wu, Prog. Mater. Sci. 57 (2012) 1–62.
[28] M.D. Uchic, D.M. Dimiduk, J.N. Florando, W.D. Nix, Science 305 (2004) 986–989.
[29] C. Ni, Q. Zhu, J. Wang, Mater. Sci. Eng. A 733 (2018) 164–169.
[30] S.H. Oh, M. Legros, D. Kiener, G. Dehm, Nat. Mater. 8 (2009) 95–100.
[31] D.M. Dimiduk, C. Woodward, R. LeSar, M.D. Uchic, Science 312 (2006) 1188–1190.
[32] T. Zhu, J. Li, A. Samanta, A. Leach, K. Gall, Phys. Rev. Lett. 100 (2008) 025502.
[33] A. Schneider, B. Clark, C. Frick, P. Gruber, E. Arzt, Mater. Sci. Eng. A 508 (2009) 241–246.
[34] D. Kiener, A.M. Minor, Acta Mater. 59 (2011) 1328–1337.
[35] Z.W. Shan, R.K. Mishra, S.A. Syed Asif, O.L. Warren, A.M. Minor, Nat. Mater. 7 (2008) 115–119.
[36] T.A. Parthasarathy, S.I. Rao, D.M. Dimiduk, M.D. Uchic, D.R. Trinkle, Scr. Mater. 56 (2007) 313–316.
[37] Z.J. Wang, Q.J. Li, Z.W. Shan, J. Li, J. Sun, E. Ma, Appl. Phys. Lett. 100 (2012).
[38] Z. Wu, Y.F. Gao, H. Bei, Scr. Mater. 109 (2015) 108–112.
[39] N.L. Okamoto, S. Fujimoto, Y. Kambara, M. Kawamura, Z.M. Chen, H. Matsunoshita, K. Tanaka, H. Inui, E.P. George, Sci. Rep. 6 (2016) 35863.
[40] M.D. Uchic, P.A. Shade, D.M. Dimiduk, Annu. Rev. Mater. Res. 39 (2009) 361–386.
[41] J.Y. Zhang, G. Liu, J. Sun, Int. J. Plast. 50 (2013) 1–17.
[42] N. Kheradmand, H. Vehoff, A. Barnoush, Acta Mater. 61 (2013) 7454–7465.
[43] K. Ng, A. Ngan, Philos. Mag. 89 (2009) 3013–3026.
[44] A. Kunz, S. Pathak, J.R. Greer, Acta Mater. 59 (2011) 4416–4424.
[45] Y. Kim, S. Lee, J.B. Jeon, Y.J. Kim, B.J. Lee, S.H. Oh, S.M. Han, Scr. Mater. 107 (2015) 5–9.
[46] P.J. Imrich, C. Kirchlechner, C. Motz, G. Dehm, Acta Mater. 73 (2014) 240–250.
[47] N.V. Malyar, J.S. Micha, G. Dehm, C. Kirchlechner, Acta Mater. 129 (2017) 91–97.
[48] R.P. Carreker, W.R. Hibbard, Acta Metall. 1 (1953) 654–663.
[49] W. Huo, H. Zhou, F. Fang, X. Hu, Z. Xie, J. Jiang, Mater. Sci. Eng. A 689 (2017) 366–369.
[50] M. Sadeghilaridjani, S. Muskeri, V. Hasannaeimi, M. Pole, S. Mukherjee, Mater. Sci. Eng. A 766 (2019) 138326.
[51] P. Yu, H. Cheng, L. Zhang, H. Zhang, Q. Jing, M. Ma, P. Liaw, G. Li, R. Liu, Mater. Sci. Eng. A 655 (2016) 283–291.
[52] V. Maier-Kiener, B. Schuh, E.P. George, H. Clemens, A. Hohenwarter, J. Mater. Res. 32 (2017) 2658–2667.
[53] T. Zhu, H. Li, N. Takata, M. Kobashi, M. Yoshino, ISIJ Int. (2019) ISIJINT-2019-2448.

[54] D. Caillard, J.L. Martin, Thermally Activated Mechanisms in Crystal Plasticity, Elsevier, 2003.
[55] A.T. Jennings, J. Li, J.R. Greer, Acta Mater. 59 (2011) 5627–5637.
[56] I. Ryu, W. Cai, W.D. Nix, H. Gao, Acta Mater. 95 (2015) 176–183.
[57] S.H. Oh, M. Legros, D. Kiener, G. Dehm, Nat. Mater. 8 (2009) 95–100.
[58] J. Hu, Z. Liu, E. Van der Giessen, Z. Zhuang, Extreme Mech. Lett. 17 (2017) 33–37.
[59] Y.N. Cui, P. Lin, Z.L. Liu, Z. Zhuang, Int. J. Plast. 55 (2014) 279–292.
[60] G. Dieter, in: Mechanical Metallurgy, Me Graw-Hill Book Co, Tokyo, Japan, 1988, pp. 275–324.
[61] S. Gangireddy, L. Kaimiao, B. Gwalani, R. Mishra, Mater. Sci. Eng. A 727 (2018) 148–159.
[62] J.P. Hirth, Metall. Trans. 3 (1972) 3047–3067.
[63] Y. Wang, A. Hamza, E. Ma, Appl. Phys. Lett. 86 (2005) 241917.
[64] J. Chen, Y. Shi, K. Lu, J. Mater. Res. 20 (2005) 2955–2959.
[65] P. Cavaliere, Prog. Mater. Sci. 51 (2006) 427–556.
[66] M. Dao, L. Lu, R. Asaro, J.T.M. De Hosson, E. Ma, Acta Mater. 55 (2007) 4041–4065.
[67] W. Huo, F. Fang, X. Liu, S. Tan, Z. Xie, J. Jiang, Appl. Phys. Lett. 114 (2019).
[68] S. Gangireddy, B. Gwalani, R.S. Mishra, Mater. Sci. Eng. A 736 (2018) 344–348.
[69] Z. Li, S. Zhao, H. Diao, P. Liaw, M. Meyers, Sci. Rep. 7 (2017) 1–8.
[70] D.H. Lee, I.C. Choi, M.Y. Seok, J. He, Z. Lu, J.Y. Suh, M. Kawasaki, T.G. Langdon, J.I. Jang, J. Mater. Res. 30 (2015) 2804–2815.
[71] E. Hall, Proc. Phys. Soc. Sect. B 64 (1951) 747.
[72] N. Kumar, Q. Ying, X. Nie, R. Mishra, Z. Tang, P. Liaw, R. Brennan, K. Doherty, K. Cho, Mater. Des. 86 (2015) 598–602.
[73] W.H. Liu, Z.P. Lu, J.Y. He, J.H. Luan, Z.J. Wang, B. Liu, Y. Liu, M.W. Chen, C.T. Liu, Acta Mater. 116 (2016) 332–342.
[74] T. Yang, Y. Zhao, Y. Tong, Z. Jiao, J. Wei, J. Cai, X. Han, D. Chen, A. Hu, J. Kai, Science 362 (2018) 933–937.
[75] J.C. Ye, Y.M. Wang, T.W. Barbee, A.V. Hamza, Appl. Phys. Lett. 100 (2012).
[76] S. Wei, S. Zheng, L. Zhang, Y. Liu, J. Wang, Mater. Res. Lett. 8 (2020) 299–306.
[77] Q. Zhu, S.C. Zhao, C. Deng, X.H. An, K.X. Song, S.X. Mao, J.W. Wang, Acta Mater. 199 (2020) 42–52.
[78] Q. Zhu, G. Cao, J. Wang, C. Deng, J. Li, Z. Zhang, S.X. Mao, Nat. Commun. 10 (2019) 156.
[79] S. Wei, Z. Zhao, S. Zheng, H. Wei, J. Wang, Scr. Mater. 190 (2021) 103–107.
[80] T. Fang, W. Li, N. Tao, K. Lu, Science 331 (2011) 1587–1590.
[81] X. Li, L. Lu, J. Li, X. Zhang, H. Gao, Nat. Rev. Mater. 5 (2020) 706–723.
[82] Q. Zhu, L. Kong, H. Lu, Q. Huang, Y. Chen, Y. Liu, W. Yang, Z. Zhang, F. Sansoz, H. Zhou, Sci. Adv. 7 (2021) eabe4758.
[83] Y. Zhao, J.M. Park, J.I. Jang, U. Ramamurty, Acta Mater. (2021) 124–134.
[84] Z.G. Zhu, X.H. An, W.J. Lu, Z.M. Li, F.L. Ng, X.Z. Liao, U. Ramamurty, S.M.L. Nai, J. Wei, Mater. Res. Lett. 7 (11) (2019) 453–459.
[85] D.H. Lee, J.A Lee, Y.K. Zhao, Z.P. Lu, J.Y. Suh, J.Y. Kim, U. Ramamurty, M. Kawasaki, T.G. Langdon, J.I. Jang, Acta Mater. 140 (2017) 443–451.
[86] N. Nayan, G. Singh, S.V.S.N. Murty, A.K. Jha, B. Pant, K.M. George, U Ramamurty, Intermetallics 55 (2014) 145–153.
[87] Y.K. Zhao, J.M. Park, D.H. Lee, E.J. Song, J.Y. Suh, U. Ramamurty, J.I. Jang, Scripta Mater. 168 (2019) 76–80.
[88] S.H. Li, W.Z Han, Z.W. Shan, Acta Mater. 141 (2017) 183–192.